Compact and Energy-Efficient Forward-Biased PN Silicon Mach-Zehnder Modulator

Sourav Dev, Karanveer Singh, Reza Hosseini, Arijit Misra, *Graduate Student Member, IEEE*, Mircea Catuneanu, Stefan Preußler, Thomas Schneider, and Kambiz Jamshidi, *Senior Member, IEEE*

***Abstract*—A compact device model along with simulations and an experimental analysis of a forward-biased PN junction-based silicon Mach-Zehnder modulator (MZM) with a phase-shifter length of 0.5 mm is presented. By placing the PN junction to a certain off-center such that 72% of the waveguide is p-doped, the refractive index swing at a given drive voltage swing is increased by 2% compared to the symmetric layout. The effects of the phase shifters' length mismatch and asymmetric splitting on the modulation efficiency and extinction ratio of the modulator are simulated and compared with experimental results. Without any pre-emphasis or post-processing, a high-speed operation up to 15 Gb/s using a non-return-to-zero modulation format is demonstrated. A modulation efficiency ($V_{\pi}L$) as low as 0.07 V $\times$ cm is verified and power consumption of 0.88 mW/Gb/s is recorded while a high extinction ratio of 33 dB is experimentally demonstrated. Compared to previously reported forward-biased silicon integrated modulators, without active tuning of the power splitting ratio between the arms, the extinction ratio is 10 dB higher. This MZM along with its compact structure is also sufficiently energy-efficient due to its low power consumption. Thus, it can be suitable for applications like analog signal processing and high-order amplitude modulation transmissions.**

***Index Terms*—Silicon photonics, photonic integrated circuits.**

I. Introduction

THE NUMBER of users and subsequently the amount of data have been increasing in communication networks in recent years. It creates the necessity to accommodate more and more devices in a single chip, which in turn requires aggressive scaling [1], [2]. In the electronic domain, devices are hitting the bandwidth scaling bottleneck and thus photonic devices are attracting immense interest [3], [4]. To bridge the gap between the electronic and photonic domains, electro-optic modulation is required. Silicon-based Mach-Zehnder modulators (MZM) are being utilized as a fundamental building block in several major photonic integrated circuits, as they can be fabricated using a complementary metal-oxide-semiconductor (CMOS) technology for large-scale integration.

The refractive index of silicon can be varied by changing the concentration of the carriers inside the material, which can be performed in two ways [5], [6]. The first is to deplete the carriers (by utilizing reverse-bias configuration) [7], [8], and the second way is to inject carriers (by a forward-bias configuration) [9]–[12]. The number of reverse-biased MZMs manufactured by the silicon industry every year is far more than the number of forward-biased MZMs as they are suitable for various applications that require high BW, high speed, etc. Although, the industry will most likely continue to use reverse-biased modulators for various applications, however, forward-biased modulators have some advantages, for example, high ER, low dynamic power consumption, and smaller size. Taking these into account, forward-biased MZMs might be used for lower bit rate applications with higher ER and power consumption requirements. Therefore, it is important to study forward-biased MZMS, so that the industry can utilize forward-biased MZMs for some niche applications based on their special properties. In recent years, the performance of silicon modulators in terms of extinction ratio (ER), insertion loss (IL), modulation efficiency (ME, expressed as $V_{\pi}L$, with V_{π} as the required voltage to achieve a phase shift of π), power consumption, and modulation speed has been improved drastically.

To further enhance the performance of a modulator in terms of ME, several structures have been proposed in the past few years [13], [14]. Resonant structures like silicon micro-ring resonators can improve the ME and therefore reduce the power consumption to a great extent, but show a higher temperature sensitivity [15]–[17]. Benefiting from slow light, modulators with corrugated structures can be used to reduce the length of the phase-shifters to provide a higher level of integration. However, providing a low insertion loss is challenging for these structures [18]–[20]. By utilizing a forward-bias configuration, the IL can be minimized along with an improved ME by sacrificing the modulation speed. The disadvantage of forward-biased modulators in terms of low speed can be compensated by using a higher-order modulation. However, a higher value of ER is necessary for this purpose. Some of the efforts to improve the ER while keeping a low IL are summarized in Table I [9], [21]–[26].

Manuscript received February 10, 2022; accepted February 14, 2022. Date of publication February 18, 2022; date of current version March 1, 2022. This work was supported in part by the Deutsche Forschungsgemeinschaft (DFG, German Research Foundation) under Grants 322402243 and 403154102, and in part by the German Federal Ministry of Education and Research (BMBF, Bundesministerium für Bildung und Forschung) under Grant 13N14879. *(Sourav Dev and Karanveer Singh contributed equally to this work.) (Corresponding author: Sourav Dev.)*

Sourav Dev, Mircea Catuneanu, and Kambiz Jamshidi are with the Integrated Photonic Devices Group, TU Dresden, 01069 Dresden, Germany (e-mail: sourav.dev@tu-dresden.de; mircea-traian.catuneanu@tu-dresden.de; kambiz.jamshidi@tu-dresden.de).

Karanveer Singh, Arijit Misra, Stefan Preußler, and Thomas Schneider are with the Terahetrtz-Photonics Group, TU Braunschweig, 38106 Braunschweig, Germany (e-mail: karanveer.singh@ihf.tu-bs.de; arijit.misra@ihf.tu-bs.de; stefan.preussler@ihf.tu-bs.de; thomas.schneider@ihf.tu-bs.de).

Reza Hosseini is with the Dassault Systèmes, 64289 Darmstadt, Hesse, Germany (e-mail: seyedreza.hosseini@3ds.com).

Digital Object Identifier 10.1109/JPHOT.2022.3152612

This work is licensed under a Creative Commons Attribution 4.0 License. For more information, see https://creativecommons.org/licenses/by/4.0/

TABLE I
COMPARISON OF THE PERFORMANCE METRICS FOR FORWARD-BIASED STANDARD MZM

Ref.	Phase shifter length (mm)	Power consumption (mW/Gb/s)	$V_\pi L$* (V×cm)	ER (dB) in DC	IL (dB)	Speed (Gb/s)
[9]	0.200	5.1	0.036	10	12	10
[21]**	0.750	1.2	0.075	N.A.	4.6	56
[22]	0.250	N.A.	0.29	23	1.2	12.5
[23]	0.250	0.6	0.1	N.A.	7.2	50
[24]	0.250	N.A.	0.024	16	N.A.	10
[25]**	0.250	1.59	1.5	N.A.	1.8	56
[26]	0.500	1.59	1.2	N.A.	N.A.	56
This work	0.500	0.88	0.07	33	2.5***	15

* V_π is the voltage required for a π phase shift.
** Including driver/equalizer.
***Calculated value (excluding grating coupler and MMI loss).

The highest ER without any active tuning reported so far is 23 dB. An established way to improve the ER further is to actively tune the power splitting ratio between the two arms of the modulator [27], [28]. However, this leads to a more complex design and increases power consumption.

In this paper, a forward-biased PN junction-based silicon MZM is designed and characterized. The compact design of this modulator with 0.5 mm of phase shifters length helps to get it integrated easily in a chip for large-scale integration. Without any optimization and active tuning, the demonstrated modulator provides an ER of 33 dB, which is 10 dB higher compared to previously reported modulators [9], [22], [24]. Moreover, this modulator offers a solution where an energy-efficient device is necessary due to its low power consumption. This silicon modulator can be employed for Nyquist pulse generation [29], [30], analog to digital conversion [30], arbitrary waveform generation [31], etc.

The paper is structured as follows. In Section II, the transfer function of the modulator is modeled. In Section III, static characteristics are simulated taking into account different arm lengths of the phase shifters and different splitting ratios for each arm and verified by comparing with the experimental results. Based on this study, the design guidelines to improve the ER of the modulator are also provided. The radio-frequency (RF) characteristics are evaluated in Section IV. Finally, the paper is concluded in Section V.

II. MATHEMATICAL MODEL OF THE MZM OPERATION

By applying an electrical field, the free carrier concentration can be changed which subsequently results in a change of the refractive index of the material. Considering the operating wavelength as 1550 nm, this change in the refractive index and the loss due to the plasma dispersion effect can be modeled as [5], [6].

$$\Delta n = -8.8 \times 10^{-22} \Delta N_{\mathrm{e}} - 8.5 \times 10^{-18} \Delta N_{\mathrm{h}}^{0.8} \quad (1)$$

$$\Delta \alpha = 8.5 \times 10^{-18} \Delta N_{\mathrm{e}} + 6 \times 10^{-18} \Delta N_{\mathrm{h}} \quad (2)$$

where Δn is the change of the real part of the refractive index, $\Delta\alpha$ is the change of the absorption coefficient, ΔN_{e} is the electron concentration and ΔN_h is the change of the hole concentration.

The real part alteration of the refractive index Δn can be used to calculate the change of the phase $\Delta\varphi$ of the light passing through the arms of the MZM as:

$$\Delta\varphi = \frac{2\pi}{\lambda_o} \Delta n L \quad (3)$$

where λ_0 is the wavelength and L is the length of the phase shifter.

The normalized power transmitted through the MZM (a function of the applied bias voltage V) can be formulated as presented in Eq. 4.

$$P_0\ (V) = \left| \frac{1}{1+\sigma} (\sigma \exp\left(-j\left(\frac{2\pi}{\lambda_o} real(n_{eff1}(V))L_1 - j\left(\frac{2\pi}{\lambda_o} imag(n_{eff1}(V))L_1\right)\right) + \exp\left(-j\left(\frac{2\pi}{\lambda_o} real(n_{eff2}(V))L_2 - j\left(\frac{2\pi}{\lambda_o} imag(n_{eff2}(V))L_2\right)\right)\right)\right|^2 \quad (4)$$

where σ is the splitting ratio (the ratio of the power in phase-shifter 1 and the power in phase shifter 2), L_1 and L_2 are the length of the two arms, n_{eff1} and n_{eff2} are their refractive indices.

III. STATIC CHARACTERIZATIONS OF THE MZM

Utilizing the model derived in Section II, the MZM is characterized by a simulation with the Lumerical DEVICE software. The cross-sectional structure of the phase shifter in the MZM is illustrated in Fig. 1(a).

The cross-section of the phase-shifter is designed to maximize the modulation efficiency of the modulator. The length of the modulator (500 μm) is chosen to maintain the required current to achieve the π phase shift within the limits of the foundry specifications. The cross-section is simulated for forward-bias voltages from 0 V to 2 V. Since the chips are fabricated using the multi-project wafer service provided by IHP microelectronics, the modulators are designed considering the standards set by them. The design is built on a silicon on insulator (SOI) substrate with a silicon layer of 220 nm with 2 μm buried oxide. The waveguide width is 460 nm, constructed with an asymmetric PN structure, having 330 nm of P-doped and 130 nm of N-doped region. The asymmetric PN structures, with a wider P-doped area, are more efficient in terms of modulation efficiency since the holes have a higher impact on the free carrier index change [32]. To evaluate this statement, the changes in the electron and hole concentrations versus the position across the PN junction, considering 1.0 V of applied DC bias voltage for three combinations of widths of the P and N doped regions for the PN junction, are presented in Fig. 2(a). In all these combinations, the total width of the WG remains the same (460 nm). The three combinations are: (i) 330 nm of P-doped and 130 nm of N-doped, (ii) 230 nm of P-doped and 230 nm of N-doped, (iii)

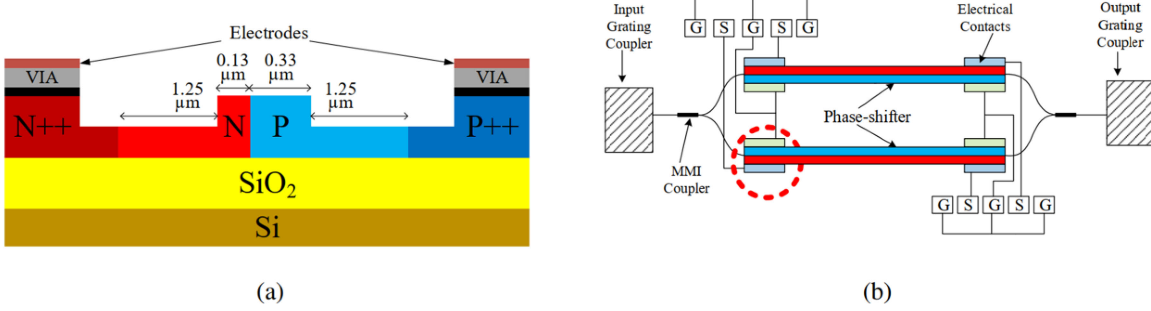

Fig. 1. (a) Cross-sectional view of the phase shifter for the fabricated MZM. (b) Top view of the circuit including the modulator. The red circle indicates where the cross-section is taken.

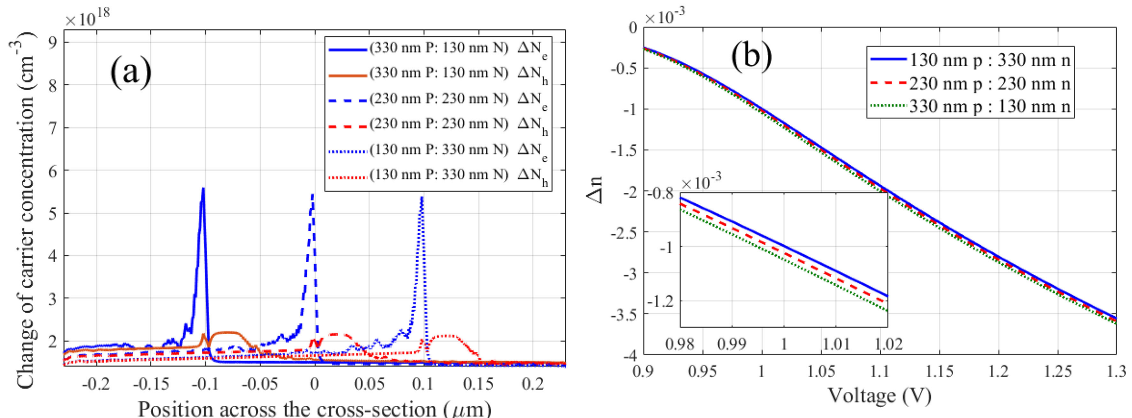

Fig. 2. (a) Simulated change of electron and hole concentrations (ΔN_e and ΔN_h respectively) versus position across the PN junction for applying 1.0 V compared to the initial concentration at 0 V. Here 0 μm means the exact middle point of the PN junction of the cross-section shown in Fig. 1(a). The WG lies between -0.23 μm to 0.23 μm; (b) Change of refractive index (Δn) for different voltages considering three PN junction combinations, the inset shows a zoomed-in image around 1.0 V.

130 nm of P-doped, and 330 nm of N-doped region. As shown in Fig. 2(a), the changes in both electron and hole concentration result in a higher number with increasing the area of the P-doped region. As stated in Eq. 1, a higher hole concentration results in a higher refractive index change. The change of the refractive index (Δn) is presented in Fig. 2(b) for the above-mentioned combinations. In the simulation, it turns out that, for combination (i) the change of the refractive index is 2% higher than the change of the refractive index considering combination (ii). Similarly, combination (ii) also offers a 2% higher change compared to combination (iii). As a result, considering the 330 nm of P-doped and 130 nm of N-doped combination, a certain change of the refractive index can be achieved for a comparatively lower voltage, thus improving the modulation efficiency.

The charge distribution in the cross-section is computed as well with the Lumerical DEVICE software package, and static simulations are performed. For N-type doping, the carrier concentration is 5×10^{18} cm^{-3}, while for P-type doping it is 7×10^{17} cm^{-3}. These carrier concentrations are chosen according to the requirements of the foundry. The parameters used in the design are selected by performing simulations considering the maximum current rating and minimum widths of the P and N-doped regions provided by the foundry. The surface recombination on the other hand is set to 10^7 cm/s as a boundary estimation.

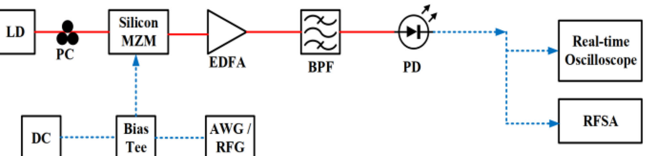

Fig. 3. Block diagram of the experimental setup for the characterization of the integrated modulator; Here, LD: laser diode, PC: polarization controller, DC: direct current source, AWG/RFG: arbitrary waveform generator or radio-frequency generator, respectively, EDFA: Erbium-doped fiber amplifier, BPF: bandpass filter, PD: photodiode, RFSA: radio-frequency spectrum analyzer. Red connection lines are optical paths and dotted blue connection lines are electrical paths.

This charge distribution was imported in the Lumerical MODE software to evaluate the mode profile and subsequently the change of the refractive index and the transmitted power, as a function of the applied bias voltage.

After the fabrication of the chips, the simulation results are verified by experiments with the setup shown in Fig. 3. An optical carrier around 1550 nm is generated using a distributed feedback laser diode. A polarization controller (PC) is used to ensure proper input polarization to the chip. To compensate for the high coupling loss, an Erbium-doped fiber amplifier (EDFA) is incorporated to amplify the output signal. A 1 nm band-pass filter

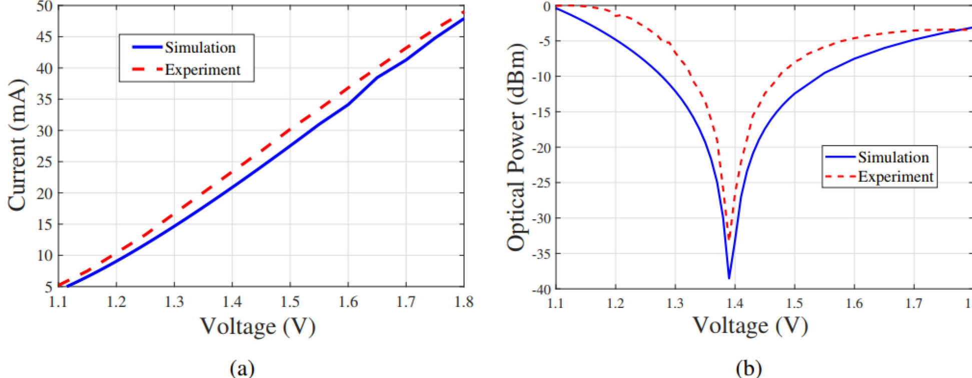

Fig. 4. DC characterization of the MZM for different bias voltages: (a) current-voltage characteristics, (b) transmitted power as a function of the applied voltage.
.

(BPF) after the amplifier mitigates the amplified spontaneous emission noise. The conversion of the signal from the optical to the electrical domain is done by a 40 GHz Optilab Photodiode. A bias tee combines the DC and input electrical signals and is fed to the chip using a ground-signal-ground-signal-ground (GSGSG) probe. As shown in Fig. 1(b), each GSGSG port is connected to both phase-shifters. During the experiment, one GSGSG probe is used and the voltage is swept using one signal port on one of the two arms at a time to create the phase difference, while the end of each phase shifter arm is terminated with a 50 Ω resistor. Fig. 4 compares the simulation and experimental results for the current-voltage (IV)-characteristics and the output optical power of the modulator.

The change of the output optical power with respect to the bias voltage is shown in Fig. 4(b). Experimental results are measured for an optical input power of 10 dBm. The modulator's optical power transfer function is measured using an optical power meter for the applied DC bias sweep. As shown in Fig. 1(b), for the designed device the metal contacts are much shorter than the phase-shifter. To increase the carrier concentration in a smaller region, the metal contacts have a total length of 40 μm or 20 μm on each side of the MZM arm. The reason for this design choice was to ensure the impedance matching for RF operations.

By solving the Poisson equation, the free carrier distribution along the phase-shifter is obtained. The simulation shows that the free carriers do not get a uniform distribution throughout the phase-shifter, instead, they are concentrated around the metal contacts. Moreover, although it was assumed during the design procedure that the lengths of both arms are the same, there are some uncertainties due to fabrication imperfections. Thus, a length mismatch can be expected, and the length of the phase-shifters might become asymmetric during the fabrication. By these mismatches, V_π and the ER might be affected. As can be seen from Fig. 4(b), for the fabricated device, a V_π of 1.4 V has been measured (dashed red curve). To incorporate the mentioned fabrication errors in the simulation procedure, simulation results with different length mismatches are swept to find the best match to the measurement result. As presented by the blue curve in Fig. 4(b), the simulation and measurement results are in good agreement with each other when the length mismatch is set to 40 nm (which is lower than the resolution set by the foundry). A high ER of 33 dB is measured. The minimum transmission occurs at the voltage and current of 1.4 V and 22 mA correspondingly (Fig. 4(a)). At this point, the simulated ER is only slightly larger than the experimental value.

In Fig. 5, L_1 and L_2 are considered to be the length of the two phase-shifters and L_1 is the actively driven arm. The output optical powers for the modulators with different phase-shifter lengths are presented here. In Fig. 5(a), both arms have the same length (symmetric phase-shifters). It can be observed from the figure that, with an increase of the length of the phase-shifter, the required voltage to achieve the transmission minima decreases, and the ER remains the same, as expected. In the inset of Fig. 5(a), the effect of the power splitting ratio between the arms (σ) on the output optical power of the modulator is presented, considering a phase-shifter with a length of 500 μm. It shows that, by increasing the value of the splitting ratio (more power at the actively driven arm), the voltage to achieve transmission minima remains almost constant, whereas the ER increases. The reason for having almost the same voltage is that the phase of the transmission response of the modulator (Eq. 4) will not be affected by the change of the splitting ratio. However, at this voltage, the excess power routed to the active arm offsets the additional dynamic losses at that arm which results in a higher ER. These simulations do not consider electrical heating due to the injected current.

To study the effect of the length mismatch, simulation results are presented for different splitting ratios (less than, equal to, and more than one) in Fig. 5(b), (c), and (d). In these figures, the length of the passive arm is kept constant to 500 μm and the length of the active arm is varied. As L_2 is the passive arm, the second term of Eq. 4 remains constant. For $L_1 < L_2$ and the same applied voltage, both the phase and the amplitude part of the first term of Eq. 4 get smaller. The reduction of the amplitude part results in a higher ER. However, the reduced values of the amplitude and phase parts of the first term contradict the total output power. Therefore, when $L_1 < L_2$, voltage for transmission minima decreases, and the ER increases. This might occur because a phase shift other than π is needed to reach it. On the other hand, for $L_1 > L_2$, voltage for transmission minima increases, and the ER decreases.

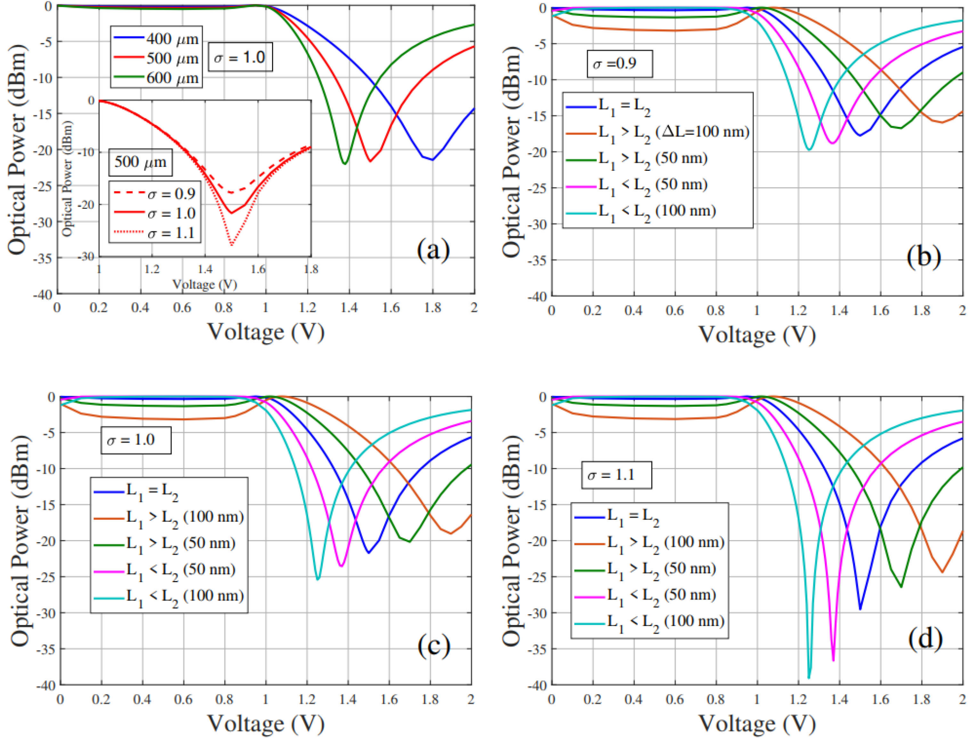

Fig. 5. Output power of the MZM vs voltage considering the effect of the length difference between the phase-shifter arms and the splitting ratio (σ), (a) for different phase-shifter lengths and $L_1 = L_2$ considering σ=1 (the inset shows the effect of the splitting ratio considering L=500 μm), (b-d) different phase-shifter length mismatches, for (b) $\sigma = 0.9$, (c) $\sigma = 1.0$, (d) $\sigma = 1.1$. In all sub-figures, L_1 is the actively driven arm.

Based on the simulations, a slight asymmetry in the phase shifter lengths can change the values of voltage for transmission minima and the ER. These simulation results can be used to achieve a better ER by utilizing an asymmetric structure. With the above design parameters, a splitting ratio of more than one and a shorter active arm result in a higher ER, whereas a shorter active arm results in a lower voltage to achieve the transmission minima This can be used as a design guideline for improving the design of the MZM with different constraints.

IV. RF Characterization of the MZM

For the RF characterization, a signal generator (Agilent technologies E8257D) is used to carry out the frequency sweep with an 18 dBm output power for the signal. The loss of the balun and bias Tee adds up to 8 dB, hence the total input electrical signal power applied to the chip is approximately 10 dBm (7 dBm to one single arm of the probe). The electrical input signal is swept for different bias voltages (0 V, 1 V, 2 V, and 2.5 V). The electro-optic response of the modulator for different bias voltages is measured using an electrical spectrum analyzer (Anritsu MS2830A) and is shown in Fig. 6(a). The electrical response of the employed bias tees, balun, and RF cables, is also measured for the same parameters with the electrical spectrum analyzer. This input circuit response is then compensated from the measured power at different biases. As can be observed from Fig. 6(a), initially the loss decreases with the value of the applied forward-bias voltage. This is clearly visible from the zoomed-in image in the inset of the figure. However, the roll-off gets faster with the increase of the bias voltage, especially noticeable after 1 GHz.

For the next step, the signal broadband operations of the device are evaluated. An arbitrary waveform generator (AWG) is used to generate a non-return-to-zero (NRZ) PRBS-7 signal. The response of the electrical input system (excluding Balun and Bias Tee) is also calibrated for the data transmission. The output of the AWG (set at 400 mVpp) is amplified using an electrical amplifier and the signal power to one arm of the probe is 5 dBm and the bias was set at 0.87 V. With a swing of 1.125 Vpp the modulator operates at the point which provides lowest BER for the data transmission. At this point, the loss becomes 1.8 dB from the peak for 15 Gb/s data transmission. This scheme minimizes the DC power consumption but at the cost of high Vpp, which increases the RF power consumption. Alternatively, the device can be operated at a bias point closer to the transmission minima, which reduces the necessary RF power at the expense of higher DC power consumption. A 20 GHz photodiode is used for electrical to optical conversion and the recorded waveforms are analyzed using a real-time oscilloscope (Tektronix DPO73304) for the visualization of the eye diagrams and symbol constellations and the measurement of error vector magnitude (EVM). A DC block is used before the receiver resulting in a negative shift of the eye diagrams. The data recorded using this receiver system is raw and provides the BER without any correction. No forward error correction (FEC) and pre-distortion are applied for the performed experiments. The signal analyses are conducted for 5 Gb/s, 10 Gb/s, and 15 Gb/s NRZ PRBS-7 modulations, and the recorded eye diagrams are presented in Fig. 6. To avoid a

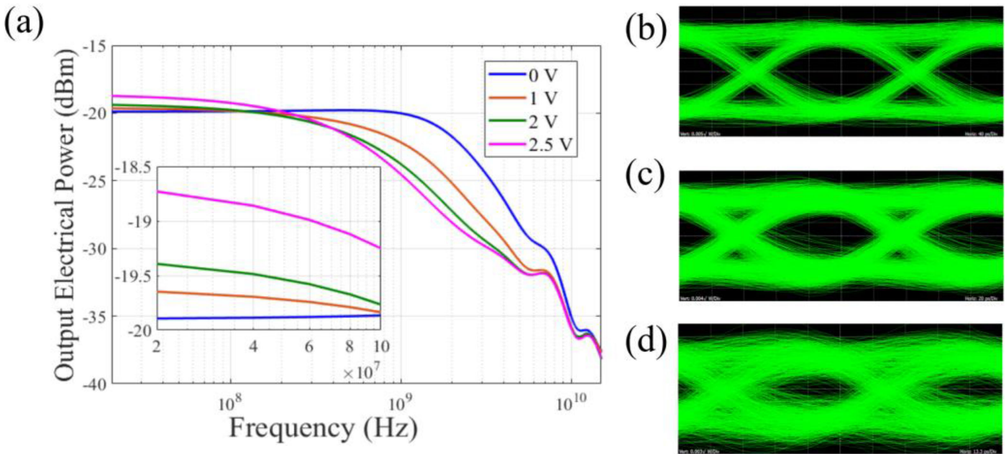

Fig. 6. (a) Measured electrical output power for different bias voltages. Measured eye-diagram for a non-return-to-zero (NRZ) PRBS-7 data modulation for different operational speeds: (b) 5 Gb/s, (c) 10 Gb/s, (d) 15 Gb/s.

TABLE II
COMPARISON OF THE PERFORMANCE METRICS

NRZ bit rate (Gb/s)	BER	EVM
5	2.42e-06	16.03 %
10	1.05e-05	17.25 %
15	2.94e-04	27 %

longer acquisition time, a limited number of bits are transmitted (100000 bits) for every speed. For 5 Gb/s and 10 Gb/s NRZ modulations, no bit error is recorded, and the BER is calculated using the measured Q-factor using Eq. 5 [33]. For 15 Gb/s a BER of $2.94\text{x}10^{-4}$ is directly recorded and is verified using the measured Q-factor. The error vector magnitude (EVM) is shown in Table II to better evaluate the performance metric for every speed. For the eye diagram measurement, the measured ER are 6.2 dB, 5.6 dB, and 5 dB at 5Gb/s, 10Gb/s, and 15 Gb/s respectively. The OMA are −5.4 dBm, −5 dBm, and −4.8 dBm respectively.

$$BER_{est} = {}^{1}\!/_{2}\, erfc\left({}^{Q}\!/_{\sqrt{2}}\right) \quad (5)$$

All these results are achieved without any pre-emphasis to the input electrical signal and the photodiode response is also not taken into account. Especially for a data transmission system, the signal needs to be adapted to the response of the electrical input (balun and bias Tee). By using the measured output response of the modulator, the pre-distortion can be applied to the data transmission files and the performance can be further enhanced. But this post-processing is not carried out for the simple device characterization and only the raw data are presented.

In every case for the output power measurement at different forward biases, the response gets a dip around 1 GHz. The low BW is expected due to the forward-bias configuration, but as a trade-off, this configuration offers an efficient power consumption. Considering 15 Gb/s speed, using IV characteristics, the calculated power consumption is 0.88 mW/Gb/s, which is sufficiently low compared to a standard reverse-biased MZM.

V. CONCLUSION

We have investigated a compact forward-biased PN junction-based silicon Mach-Zehnder modulator with an extinction ratio of 33 dB that is higher than comparable integrated silicon modulators while keeping the modulator's insertion loss within a considerable limit (calculated as 2.5 dB excluding the grating coupler and MMI loss). Although the BW of the modulator is comparatively low due to the design based on the forward-biased junction, the modulator is energy efficient and has a modulation efficiency ($V_\pi L$) which is measured to be 0.07 V×cm. It also offers a low power consumption which is calculated to be 0.88 mW/Gb/s. The effects of the phase-shifters length mismatch (asymmetry) and different split ratios on the ER and the voltage required for transmission minima are simulated. While different parameters can affect these values like phase-shifter length mismatch, homogeneity of doping, waveguide roughness, etc., but we considered a simplified model to study the length mismatch only while other parameters remain unaffected. From this model, the simulated results fit the experimental results best when a length difference of 40 nm between the arms is considered. We have also presented the design guidelines to improve the ER of the modulator, which might help to optimize the structure accordingly. Without any post-processing or pre-emphasis, an NRZ optical modulation of 15 Gb/s is measured. Due to its compact and low energy-consumption characteristics, the modulator design is especially suitable for applications where compact, low insertion loss, and low modulation efficiency modulators are required.

REFERENCES

[1] G. E. Moore, "Cramming more components onto integrated circuits, reprinted from electronics, volume 38, number 8, april 19, 1965, pp.114 ff," *IEEE Solid-State Circuits Soc. Newslett.*, vol. 11, no. 3, pp. 33–35, Sep. 2006.

[2] G. P. Fettweis *et al.*, "Architecture and advanced electronics pathways toward highly adaptive energy- efficient computing," in *Proc. IEEE*, 2019, vol. 107, no. 1, pp. 204–231.

[3] O. Gerstel, M. Jinno, A. Lord, and S. Yoo, “Elastic optical networking: A new dawn for the optical layer?,” *IEEE Commun. Mag.*, vol. 50, no. 2, pp. s12–s20, Feb. 2012.

[4] G. Lifante, *Integrated Photonics: Fundamentals*. Hoboken, NJ, USA: Wiley, 2003.

[5] R. Soref and B. Bennett, “Electrooptical effects in silicon,” *IEEE J. Quantum Electron.*, vol. QE-23, no. 1, pp. 123–129, Jan. 1987.

[6] M. Nedeljkovic, R. Soref, and G. Z. Mashanovich, “Free-carrier electrorefraction and electroabsorption modulation predictions for silicon over the 1–14- ‘m infrared wavelength range,” *IEEE Photon. J.,* vol. 3, no. 6, pp. 1171–1180, Dec. 2011.

[7] O. Jafari, W. Shi, and S. Larochelle, “Mach-Zehnder silicon photonic modulator assisted by phase-shifted Bragg gratings,” *IEEE Photon. Technol. Lett.*, vol. 32, no. 8, pp. 445–448, Apr. 2020.

[8] M. Passoni, D. Gerace, L. O’Faolain, and L. C. Andreani, “Slow light with interleaved p-n junction to enhance performance of integrated Mach-Zehnder silicon modulators,” *Nanophotonics*, vol. 8, pp. 1485–1494, 2019.

[9] W. M. Green, M. J. Rooks, L. Sekaric, and Y. A. Vlasov, “Ultra-compact, low RF power, 10 gb/s silicon Mach Zehnder modulator,” *Opt. Exp.*, vol. 15 2007, Art. no. 17106.

[10] R. L. Chao *et al.*, “Forward bias operation of silicon photonic Mach Zehnder modulators for RF applications,” *Opt. Exp.*, vol. 25, 2017, Art. no. 23181.

[11] R. Hosseini, L. Mirzoyan, and K. Jamshidi, “Energy consumption enhancement of reverse-biased silicon-based Mach–Zehnder modulators using corrugated slow light waveguides,” *IEEE Photon. J.*, vol. 10, no. 1, Feb. 2018, Art. no. 8200207.

[12] F. Gan and F. Ka, “High-speed silicon electrooptic modulator design,” *IEEE Photon. Technol. Lett.*, vol. 17, no. 5, pp. 1007–1009, May 2005.

[13] G. T. Reed, G. Mashanovich, F. Y. Gardes, and D. J. Thomson, “Silicon optical modulators,” *Nat. Photon.*, vol. 4, pp. 518–526, 2010.

[14] J. Witzens, “High-speed silicon photonics modulators,” in *Proc. IEEE*, 2018, vol. 106, pp. 2158–2182.

[15] Q. Xu, S. Manipatruni, B. Schmidt, J. Shakya, and M. Lipson, “12.5 gbit/s carrier-injection-based silicon micro ring silicon modulators,” *Opt. Exp.*, vol. 15, pp. 430–436, 2007.

[16] K. Padmaraju and K. Bergman, “Resolving the thermal challenges for silicon microring resonator devices,” *Nanophotonics*, vol. 3, pp. 269–281, 2014.

[17] M. R. Watts, D. C. Trotter, R. W. Young, and A. L. Lentine, “Ultralow power silicon microdisk modulators and switches,” in *Proc. 5th IEEE Int. Conf. Group IV Photon.*, 2008, pp. 4–6.

[18] R. Hosseini *et al.*, “Compact, high extinction ratio silicon Mach-Zehnder modulator with corrugated waveguides,” in *Proc. Conf. Lasers Electro-Opt.*, 2018, pp. 1–2.

[19] A. Brimont *et al.*, “High speed silicon electro-optical modulators enhanced via slow light propagation,” *Opt. Exp.*, vol. 19, 2011, Art. no. 20876.

[20] Y. Hinakura, H. Arai, and T. Baba, “64 gbps si photonic crystal slow light modulator by electro-optic phase matching,” *Opt. Exp.*, vol. 27, 2019, Art. no. 14321.

[21] S. Tanaka, T. Usuki, and Y. Tanaka, “Accurate SPICE model of forward-biased silicon PIN Mach–Zehnder modulator for an energy-efficient multilevel transmitter,” *J. Lightw. Technol.*, vol. 36, no. 10, pp. 1959–1969, May 2018.

[22] S. Akiyama *et al.*, “12.5-gb/s operation with 029-v·cm v_πl using silicon Mach-Zehnder modulator based-on forward-biased pin diode,” *Opt. Exp.*, vol. 20, 2012, Art. no. 2911.

[23] S. Akiyama *et al.*, “Compact PIN-diode-based silicon modulator using side-wall-grating waveguide,” *IEEE J. Sel. Top. Quantum Electron.*, vol. 19, no. 6, pp. 74–84, Nov./Dec. 2013.

[24] G. R. Zhou *et al.*, “Effect of carrier lifetime on forward-biased silicon Mach-Zehnder modulators,” *Opt. Exp.*, vol. 16, 2008, Art. no. 5218.

[25] S. Tanaka *et al.*, “Ultralow-power (1.59 mW/gbps), 56-gbps PAM4 operation of si photonic transmitter integrating segmented PIN Mach–Zehnder modulator and 28-nm CMOS driver,” *J. Lightw. Technol.*, vol. 36, no. 5, pp. 1275–1280, Mar. 2018.

[26] S. Tanaka and Y. Sobu, “High-speed silicon photonic modulator based on forward-biased PIN diodes and passive equalizers,” in *Proc. Eur. Conf. Opt. Commun.*, 2020, pp. 1–4.

[27] Y. Yamaguchi, S. Nakajima, H. Nakajima, M. Izutsu, A. Kanno, and T. Kawanishi, “Single Mach-Zehnder modulator with active Y-branch for higher than 60 dB extinction-ratio operation,” in *Proc. 39th Eur. Conf. Exhib. Opt. Commun.*, 2013, pp. 1–3.

[28] T. Kawanishi, T. Sakamoto, A. Chiba, and M. Izutsu, “Study of precise optical modulation using Mach-Zehnder interferometers for advanced modulation formats,” in *Proc. 33rd Eur. Conf. Exhib. Opt. Commun.*, 2007, pp. 1–2.

[29] M. A. Soto *et al.*, “Optical sinc-shapednyquist pulses of exceptional quality,” *Nat. Commun.*, vol. 4, 2013, Art. no. 2898.

[30] A. Misra, C. Kress, K. Singh, S. Preußler, J. C. Scheytt, and T. Schneider, “Integrated source-free all optical samplingwith a sampling rate of up to three times the rf bandwidth of silicon photonic mzm,” *Opt. Exp.*, vol. 27, pp. 29972–29984, 2019.

[31] K. Singh, J. Meier, A. Misra, S. Preußler, J. C. Scheytt, and T. Schneider, “Photonic arbitrary waveform generation with three times the sampling rate of the modulator bandwidth,” *IEEE Photon. Technol. Lett.*, vol. 32, no. 24, pp. 1544–1547, Dec. 2020.

[32] A. Abraham *et al.*, “Optimization of silicon MZM fabrication parameters for high speed short reach interconnects at 1310 nm,” *Appl. Sci.*, vol. 6, 2016, Art. no. 395.

[33] W. Freude *et al.*, “Quality metrics for optical signals: Eye diagram, Q-factor, OSNR, EVM and BER,” in *Proc. 14th Int. Conf. Transparent Opt. Netw.*, 2012, pp. 1–4.